GEOLOGICAL SURVEY OF CANADA
OPEN FILE 8756

3-D mantle structure of the Superior Craton

**D.B. Snyder, A. Vaillancourt, B.A. Kjarsgaard,
G. Savard, and E.A. de Kemp**

2024

Canada

3-D mantle structure of the Superior Craton

D.B Snyder[1], A. Vaillancourt[1], B.A. Kjarsgaard[1], G. Savard[2], and E.A. de Kemp[1]

[1]Geological Survey of Canada, 601 Booth Street, Ottawa, Canada
[2]Department of Geoscience, University of Calgary, 2500 University Drive N.W., Calgary, Alberta

2024

Contents

Figures:

Tables:

Appendices:

Abstract

New 3D multi-azimuthal receiver function analysis identified four regional seismic discontinuities dipping at 7–13° within the mantle of the Superior craton of North America; most are discordant to known major upper crustal structures. Widely observed crustal-scale structures with near vertical axial planes striking east-west indicate that the most recent and dominant phase of folding and horizontal shortening strain occurred during the Kenoran (D2) crustal deformation concurrent with Au-mineralization and peak metamorphism at 2.72–2.66 Ga. Two mantle discontinuities strike 065° and 249°, dipping to the southeast and northwest, respectively. These strike roughly parallel the northern margin of the Superior craton and some intra-cratonic features such as the axis of the Quetico Basin.

Two discontinuities strike 355° and 187°, dipping to the east and west, respectively, and parallel to the western margin of the craton. Our new observations reveal neither moderately dipping, east-west striking discontinuities nor coherent eclogitic layers characteristic of modern plate tectonic subduction zones. Prominent east- and west-dipping mantle structures relate best to a Paleoproterozoic (Trans-Hudson) deformation, which is rarely observed in the crust. A new analysis of mantle xenoliths and xenocrysts indicates that carbonatitic metasomatism predominates above some discontinuities where strongly localized conductivity occurs whereas kimberlitic metasomatism predominates below the discontinuities in the broadly conductive mantle.

This open file is accompanied by the 3D GOCAD geophysical data set and resultant interpreted surface models from this integration study.

1) Introduction

Structure within the Earth is best studied in three dimensions and using several coincident overlays of information with which one can best see where anomalous properties correlate. Here we use regional-scale seismic-wave discontinuity surfaces about a few hundred kilometers deep in the Earth, intersected and thus calibrated by rebuilt rock columns using sparse rock samples erupted to the surface in two locations. Electrically conductive regions can be mapped using natural (magnetotelluric) currents. East- and west-dipping seismic discontinuity surfaces match surface structures that developed about 1.8 billion years ago marginal to the Superior crustal block. Surfaces dipping to the southeast and northwest match some boundaries between crustal blocks that are over 2.5 billion years old, but many more such crustal boundaries trend east-west. Conductive rocks appear locally more common above these surfaces where gas-rich fluids apparently flowed and that the discontinuities somehow filtered these fluids. The mismatch in orientation and dip between ancient deep and exposed structures suggests that plate tectonic processes operating today differed earlier than 2.5 billion years ago. Identifying mantle structures within the Superior craton helps to identify potential zones of mineralization and further exploration targets.

The structure of the ancient continental lithosphere such as the Superior craton of North America is best understood by considering cumulative strains within the entire lithosphere, not just the upper crust. Although isotopic dating indicates that the earliest cratonic crust and mantle formed together, discordant large-scale structural trends suggest more complicated histories for the lithosphere as a whole (e.g., Grutter et al., 1999; Snyder et al., 2014).

The world's largest exposure of Archean continental crust, the Superior craton in central North America, is composed of east-west striking terranes that have served as an archetype for the uniformitarian accretion of Archean terranes above subduction zones (Daigneault et al., 2002; Langford & Morin, 1976; Percival et al., 2006; White et al., 2003). This style of tectonic amalgamation derives primarily from the long, narrow geometry of mapped terranes, the 'similarity' of Archean and modern arc geochemical signatures, and the postulated southward younging of volcanic and plutonic ages and their terrane-bounding shear zones. A number of features at variance with the subduction interpretation include the scarcity of orogenic andesites and ophiolites, and the intercalation of or close intermingling of broadly coeval plume-related komatiites with presumed subduction-related calc-alkaline volcanic and plutonic units (e.g., Bedard et al., 2013). The inferred 40–50 million years duration of arc volcanism imply that at least 600 km of oceanic lithosphere was subducted, assuming modern plate motion rates of ~10 km/Ma and normal geometries, however, very few unequivocal remnants of this vast intervening ocean floor remain (Bedard & Harris, 2014). Uncommonly the Superior has an older crust surrounding its center, a relationship inconsistent with the outward younging of modern convergent margins and previously postulated models.

Here, for the first time in the Superior craton, we identify discrete structures in the entire crust and mantle lithosphere as a whole. This is important in that the cool cratonic lithosphere is strongest at 70–100 km depths within the upper mantle, although this lithosphere was warmer and thinner when it experienced most of its early strain deformation (Bao & Eaton, 2015; Wang et al., 2014). New geophysical and geochemical observations of the mantle augment interpretations inherited from several decades of crustal research to revise the structural model and hence the tectonic-metasomatic history of the central Superior craton lithosphere. When combined in a 3D model, the new data should reveal evidence of the proposed multiple eastwest striking subduction zones with moderate to steep (30°–90°) southward dips at depths of 100–300 km. Xenoliths/xenocrysts should include samples or evidence of stratified eclogite layers derived from the subducted oceanic crust (Aulbach et al., 2020; Eeken et al., 2020). Mantle seismic discontinuities should have some characteristics of modern intra-continental subduction/collision zones (e.g., Schneider et al., 2013).

2) Data sources

Several new data acquisitions relevant to lithospheric structure have occurred in the central Superior craton (Fig. 1) since the Lithoprobe program and subsequent synthesis of its data (Percival, 2012). More uniformly spaced arrays of teleseismic stations were established by the USArray and POLARIS programs in neighbouring parts of the USA and Canada, respectively (Frederikson et al., 2007; Schaeffer and Lebedev, 2014). Two new data sets described here augment existing data to build new 3D (GOCAD) mantle models. Multi-azimuthal receiver functions revealed several mantle discontinuity surfaces. Mantle structures were derived from seismic discontinuities using 18 seismic stations in the western Superior craton (Table 1, Fig 1.) New analysis of xenocrysts revealed more consistent depth control on lithologies at two locations in the Superior craton: Kirkland Lake and Attawapiskat (Fig. 1). 3D analysis with 3D GIS tools for visualization, interpretation, and integration of all data types, that was previously more difficult, is now common and becoming standard (e.g., Snyder et al., 2014).
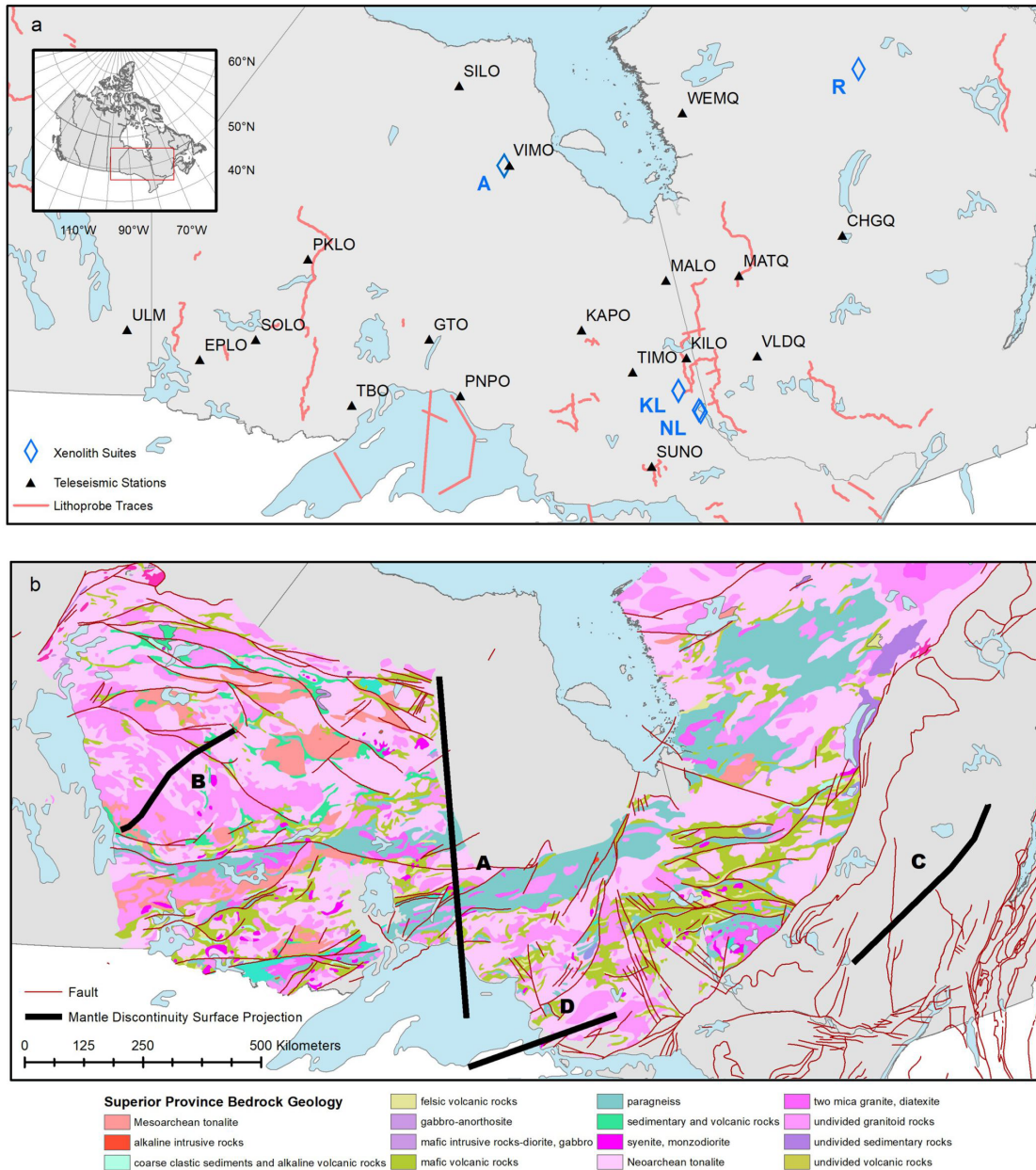
Figure 1(a, b): Red rectangle in upper left inset shows the area of interest for both maps. (a). shows the location of the teleseismic stations included in the study as black triangles. Blue diamonds show the locations of key xenolith suites: A is Attawapiskat, KL is Kirkland Lake, NL is New Liskeard, R is Renaud. Lithoprobe seismic profile traces are shown in pink. (b) shows Superior Province bedrock geology map created using data derived from Wheeler et al. 1996. Thick black lines show the surface projection of the four main mantle seismic discontinuities discussed in the text.

Table 1: *Geographic locations, earthquake counts and Moho depth estimations for Superior seismic stations*

Station	Location	Year begin	Year end	Seismic network	Latitude	Longitude	Elevation (m)	Number of events	Number of events used	Moho range (km)	EARS Moho (km)
ULM	Lac du Bonnet	1994	2018	CNSN	50.25026	-95.87495	250	990	756	35.2-37.6, 36.7.±0.5	34±0.1
EPLO	Exploration Lake	2004	2018	CNSN	49.6737	-93.72582	437	764	443	39.4-46.8, 42.1.±1.8	38±0.2
SOLO	Sioux Lookout	1998	2018	CNSN	50.0213	-92.0812	373	58	40	42.6-45.6, 44.0.±1.5	42±5
PKLO	Pickle Lake	2004	2018	CNSN	51.49867	-90.35219	376	591	428	40.0-44.5, 42.6.±1.5	39±0.3
TBO	Thunder Bay	1993	2017	CNSN	48.64718	-89.4085	475	182	125	43.9-48.3, 46.0.±1.5	44±0.5
GTO	Geraldton	2001	2018	CNSN	49.745	-86.9617	350	221	152	38.9-44.5, 40.9.±1.5	39±0.2
PNPO	Pukaskwa	2004	2018	CNSN	48.59568	-86.28463	219	507	358	45.9-49.2, 47.3.±1.4	30±1.6, 45
SILO	Sutton Inlier	2003	2018	CNSN	54.47918	-84.91262	195	254	213	41.0-43.5, 41.9.±0.6	37±8
VIMO	Victor Mine	2003	2018	CNSN	52.81726	-83.74489	78	758	578	46.7-51.5, 49.4.±1.9	42±5
KAPO	Kapuskasing	1998	2018	CNSN	49.45098	-82.50769	221	1094	944	45.7-55.3, 50.4.±2.8	48±2.1
SUNO	Sudbury Onaping	2003	2018	CNSN	46.6438	-81.3442	343	553	459	34.2-43.6, 39.3.±0.5	35±0.9
TIMO	Timmins	2005	2010	CNSN	48.46587	-81.30321	392	425	297	45.0-53.0, 48.6.±2.2	41±1.7 (D49A)
MALO	MacAlpine Lake	2013	2018	CNSN	50.0244	-79.7635	271	619	353	42.8-44.1, 44.2±1.2	39±4.5
KILO	Kirkland Lake	2003	2018	CNSN	48.4972	-79.7232	314	603	391	41.1-47.0, 43.0.±2.0	30±4.1, 36±3.6
WEMQ	Wemindji	2007	2018	POLARIS	53.0535	-77.9737	172	631	445	41.8-45.6, 43.9.±1.1	35±1.4 NMSQ
VLDQ	Val d'Or	2002	2018	CNSN	48.19014	-77.75723	316	722	541	35.6-41.0, 37.9.±1.6	35±0.2
MATQ	Matagami	2007	2018	POLARIS	49.75891	-77.63763	280	554	416		36±1.8
CHGQ	Chibougamau	2007	2018	POLARIS	49.9105	-74.37483	406	983	411	33.4-38.5, 35.6.±1.6	35±1.2

3) Methods

a) 3D Modelling overview

Seismic, Magnetotelluric (MT), structural and geochemistry data are typically processed independently and then interpreted separately without consideration of common geologic processes. Recent qualitative comparison of upper crustal 2D conductivity models derived from MT with seismic reflection profiles across a region of Archean-Proterozoic rocks in southern Australia found a spatial association between regions of low reflectivity or low velocity in seismic sections and low resistivity in MT sections (Skirrow et al., 2018). A diffuse combined seismic-MT signature signifies fossil melting of the crust, magma movement or hydrothermal fluid flow through the crust from mantle reservoirs (Roots et. al. 2022). Here we combine not just different techniques, but also application at all scales relevant to the lithosphere. Compilation of co-registered data makes it able to be viewed more naturally in stereo, with various 3D applications, which enhances the interpretability of the Superior data at craton scales.

b) Receiver function methods

Ps phase correlations (receiver functions) (Bostock, 1989) were used to build 3D surfaces where Ps phase conversions occurred. Earthquakes with magnitudes greater than 5.5 and 30° < Angular Distance < 90° were considered. Among the eighteen stations (Table 1) used in the study, 7350 of 10509 recorded earthquakes were considered of good quality to build correlations.

The multi-azimuthal maps of correlation strength were first studied as plots of depth (phase delay) versus back-azimuth of both the radial and transverse components. Radial components were used only to estimate Moho depths; transverse components for all mantle discontinuities (Figure 2). Weak Moho signatures on the transverse components reduces contamination of later phases by Moho reverberations (multiples). Data was also examined for possible multiples as depth versus distance plots (Bostock, 1989). The correlated trace for each back azimuth was then projected in 3D using ray

parameters to produce the 3D cones used in the mapping (Figure 3). The limited recording period available as well as the natural distribution of source earthquakes resulted in gaps in back azimuthal coverage, sometimes spanning tens of degrees at non-permanent stations. Here we show a few examples of phase correlations observed on radial and transverse components of four stations (Figure 2). Receiver functions from 18 stations from the POLARIS seismic network and Canadian National Seismograph Network were used in the model. Conversions from discrete back azimuths were averaged to form a ring of interpretational picks around the cones representing point estimates of a seismic discontinuity beneath the stations.

The cones were then reprojected from a geographic coordinate system to a Lambert Conformal Conic projection in accordance with the Canada in 3D model (de Kemp et al. 2022 and Appendix A1). The cones were displayed in GOCAD, and used to identify continuous features around the radius of the cone at depth (Figure 3). First we created a medium plane to extend each surface to surrounding cones. If similar features were discovered in the adjacent cones, picks would be added to the dataset. Once all possible cones were exhausted, another feature would be identified and processed as previously described. Using the points gathered, a final medium plane was created for each surface.

The points would then be used as constraints to deform the medium plane to a best-fitting undulating surface. These surfaces were inspected against the "drill holes" as a check, as well as Lithoprobe seismic profile data.
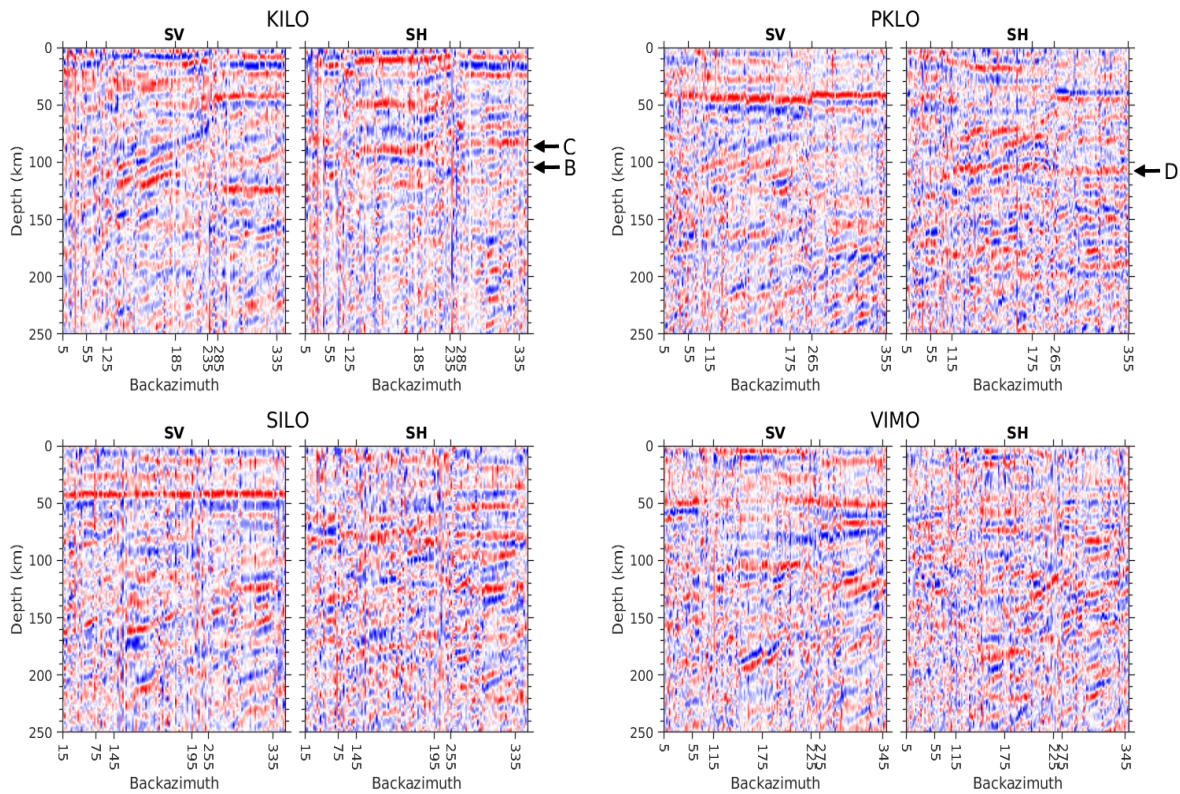

Figure 2: Radial (SV) and transverse (SH) components of the receiver functions from stations KILO, PKLO, SILO, and VIMO, filtered at 0.05-0.4 Hz. Several regionally observed discontinuities (B,C and D) are labelled. Numbers at the bottom indicate back azimuths where sufficient earthquakes contributed, in order to perform the analysis, and are thus irregularly spaced.

c) Mantle stratigraphy methods

The following provides the methodology and data sources utilized to generate: (1) a paleogeotherm and estimate of the lithosphere-asthenosphere boundary (LAB); (2) a peridotite garnet xenocryst mantle lithology classification; (3) a peridotite garnet xenocryst depletion and fluid metasomatism classification (4) a peridotite garnet xenocryst melt metasomatism classification; (5) a peridotite garnet xenocryst temperature determination, and the temperature to depth conversion; (6) composite mantle stratigraphic logs.

(1) The paleogeotherm for each kimberlite field was determined using pressure (P) and temperature (T) determinations derived from equilibrated (via established screening methods) mantle peridotite xenoliths, or Cr-diopside xenocrysts. The peridotite garnet xenocryst major and trace element data sets for Kirkland Lake, New Liskeard, Attawapiskat and Kyle Lake are from Griffin et al., (2004). Major element data used electron microprobe analysis and trace element data used laser ablation ICP-MS. For Kyle Lake the Ni data was determined by the proton induced X-ray excitation (PIXE; 'proton microprobe') method. See Griffin et al. (2004) and references therein for further analytical method details. Data sources for each kimberlite field paleogeotherm are listed in Table 2 below. This data was utilized as input parameters for the FITPLOT paleogeotherm program (Mather et al. 2011). The lithosphere-asthenosphere boundary (LAB, in km, with uncertainty) estimated using FITPLOT is also listed in Table 2.
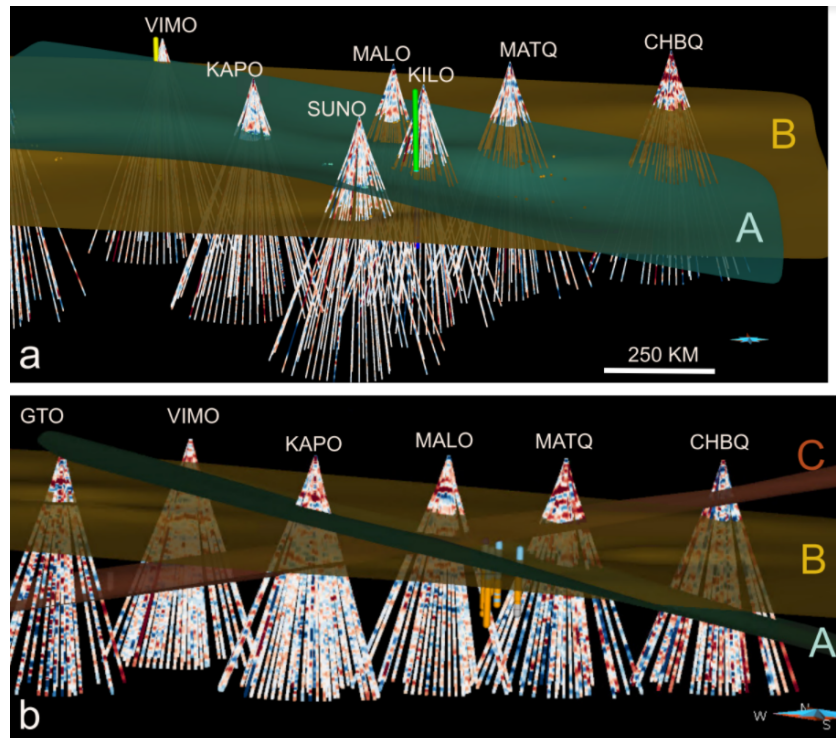
Figure 3: Mantle teleseismic discontinuity surfaces as determined from 3-D receiver function analysis in the Abitibi (southeastern) part of the Superior craton. View is to the north. The three dipping surfaces (A,B,C) were mapped from 3-D receiver function 'cones' (e.g., stations VIMO, KAPO) are shown and stations listed in Table 1; apex is at the topographic surface. Vertical columns near VIMO and KILO are 'drill holes' constructed from xenolith and xenocryst suites from the Attawapiskat and Kirkland Lake kimberlite clusters.

Table 2: Lithosphere-asthenosphere boundary (LAB), depth estimates from kimberlite fields.

Kimberlite Field	Age (Ma)	Input Type	Data Source	FITPLOT LAB
New Liskeard	127 - 155	Cr-diopside	Sage, 2000a	172 +/- 6 km
Kirkland Lake	145 - 165	Xenolith	Vickers, 1994	189 +/- 11 km
Attawapiskat	175 - 180	Xenolith	Smit et al., 2014	203 +/- 7 km
Renard	630 - 655	Xenolith	Hunt et al., 2012	227 +/- 9 km
Kyle Lake	1110	Cr-diopside	Sage, 2000b	190 +/- 11 km

(2) Mantle peridotite-derived garnet xenocryst grains (with > 1 wt% Cr_2O_3) were classified into mantle lithology parageneses based on their CaO - Cr_2O_3 concentration levels. The peridotite garnet classification utilized herein applies aspects of previously published classification systems, including those of: Sobolev (1971), Gurney (1984), Grutter et al. (2004) and Preston et al. (2012). Peridotite garnet xenocryst grains are classified as being derived from harzburgite (G10), lherzolite (G9), or wehrlite (G12) parageneses, with the harzburgite and lherzolite fields being further subdivided into very-low Ca harzburgite (G10a) and harzburgite (G10b), and low Ca lherzolite (G9a) and lherzolite (G9), respectively (Figure 4a). A constant slope of 0.30 in CaO/ Cr_2O_3 space (or 3.33 in Cr_2O_3/CaO space) is used for the four discrimination lines (Figure 4), which have CaO intercepts (i.e. y axis at 0 wt% Cr_2O_3) of 1.6 (separating G10a/G10b), 3.0 (separating G10b/G9a), 4.1 (separating G9a/G9b), and 5.4 (separating G9b/G12).
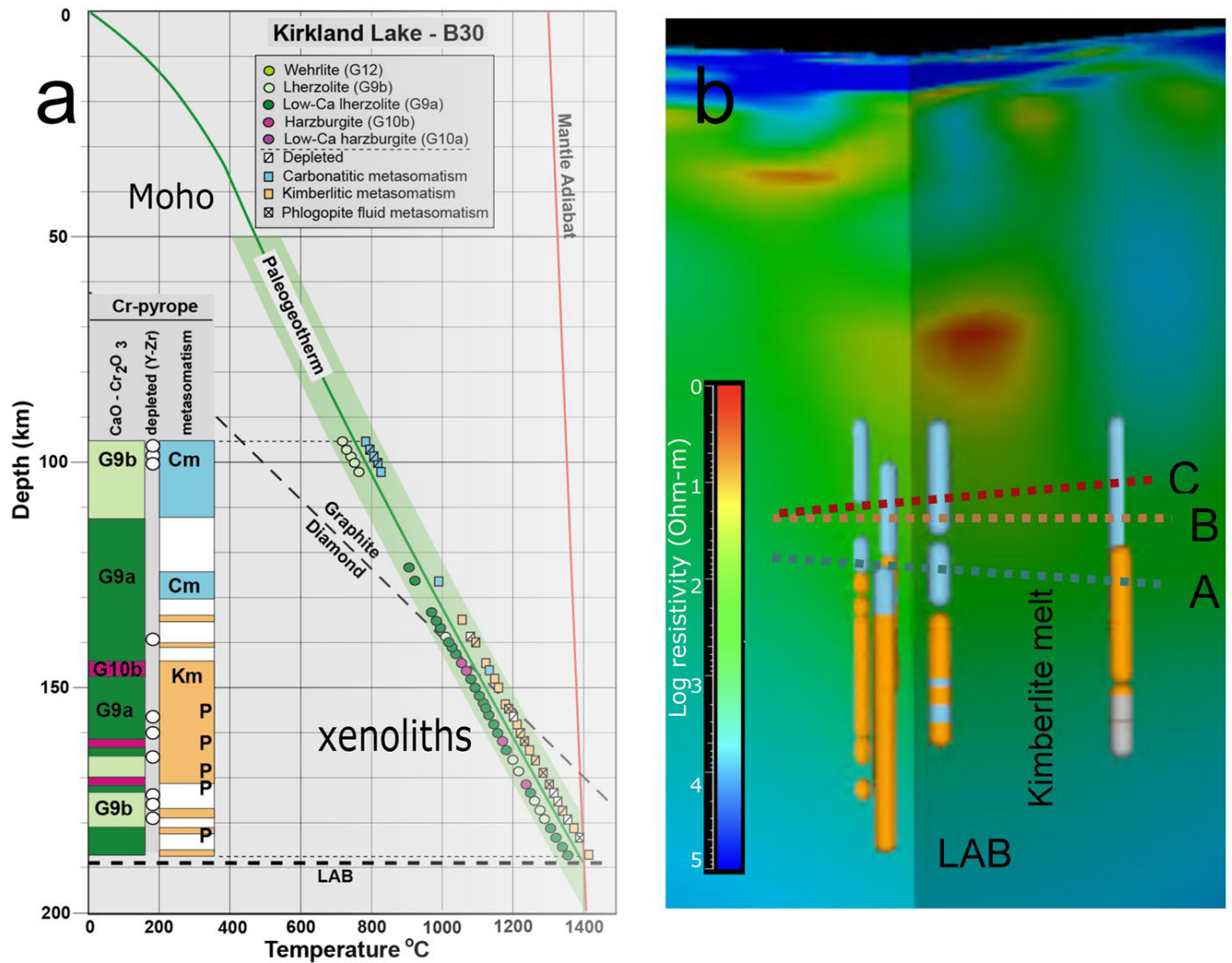
Figure 4. *Analysis of geochemical data from xenoliths and xenocrysts from kimberlites near Kirkland Lake, Ontario (KL in Figure 1). (a) FITPLOT (Mather et al., 2011) derived paleogeotherm calculated using mantle xenolith P-T data recovered from four kimberlites. The base of the lithosphere (LAB) is 189 ± 11 km depth (the intersection of the paleogeotherm and the mantle adiabat). Graphite/diamond transition is shown as a thin dashed line. Inset shows mantle stratigraphic logs of lithology type and a metasomatic overprint for kimberlite B30, based on major- and trace element geochemistry of garnet xenocrysts, respectively. G9b is lherzolite, G9a depleted lherzolite; G10b harzburgite; Km kimberlitic melt-, Cm carbonatitic melt-, P phlogopite fluid-metasomatism. See Supplementary material S2 for additional details. Data for a subset of individual garnet xenocrysts are also shown as a drape on the paleogeotherm. (b) Detail of the four Kirkland Lake metasomatism logs (blue = carbonatitic; orange = kimberlitic) compared in 3D with an MT conductivity model and three seismic discontinuities. Note the limited depth sampling range of 95–200 km available using Cr-pyrope garnet xenocrysts. A "corner" within the 3-D conductivity model is shown with an east-west cross-section (left) and a north-south one. Depth scale as in (a).*

(3) The mantle peridotite-derived garnet xenocryst grains were classified utilizing a Y- Zr discriminant plot (e.g. Griffin et al., 2004) as being depleted, or metasomatized by phlogopite fluids (Figure 4b). Further classification of melt metasomatism is done in Step 4 (below).

(4) The mantle peridotite-derived garnet xenocryst grains were classified from a mantle metasomatism perspective utilizing the Ti/Eu versus Zr/Hf discrimination diagram of Shu and Brey (2015). This classification distinguishes carbonatitic metasomatic (CM) and kimberlitic metasomatic (KM) overprinting of the peridotite garnet xenocryst grains (Figure 4a). Note that a number of garnets in this

study have higher Ti/Eu ratios (with similar Zr/Hf ratios) as compared to the work of Shu and Brey (2015). However, these grains are considered to be kimberlitic metasomatized, based on results of the "Ti-test" of Grutter et al. (2004) for distinguishing G11 (high-Ti) Cr-pyrope garnets.

(5) Peridotite garnet xenocryst temperatures were determined via Ni in garnet thermometry, with olivine having a commonly assumed Ni concentration of 2900 ppm. Temperatures were determined using the calibrations of Ryan et al (1996) and Canil (1999); these two temperatures were then averaged, as per a similar tactic used by Shu and Brey (2015). The garnet xenocryst depth was subsequently determined based on the intersection of the Ni in garnet temperature with the FITPLOT geotherm.

(6) Mantle stratigraphic logs are based on the garnet xenocryst Ca- Cr lithology paragenetic type (e.g. G9b, lherzolite), the Y-Zr depletion and fluid metasomatism classification, and the melt metasomatic overprint (e.g. kimberlitic metasomatism, or absence thereof). Separate lithology and metasomatism logs were used to allow for visualization comparison with mantle teleseismic and MT images, respectively. A simplified approach is taken with respect to the visualization of the data, based on a number of factors. For many sample suites there are < 75 garnet xenocryst samples per kimberlite locality, and furthermore the number of garnet xenocrysts is quite variable with temperature (i.e. depth) and thus sampling density. "Breaks" in the stratigraphy are located based on a simple average of the depths of two different adjacent lithology or metasomatic types, the resulting average defines the base of the overlying unit and the top of the underlying unit (Figures 5 and 6).
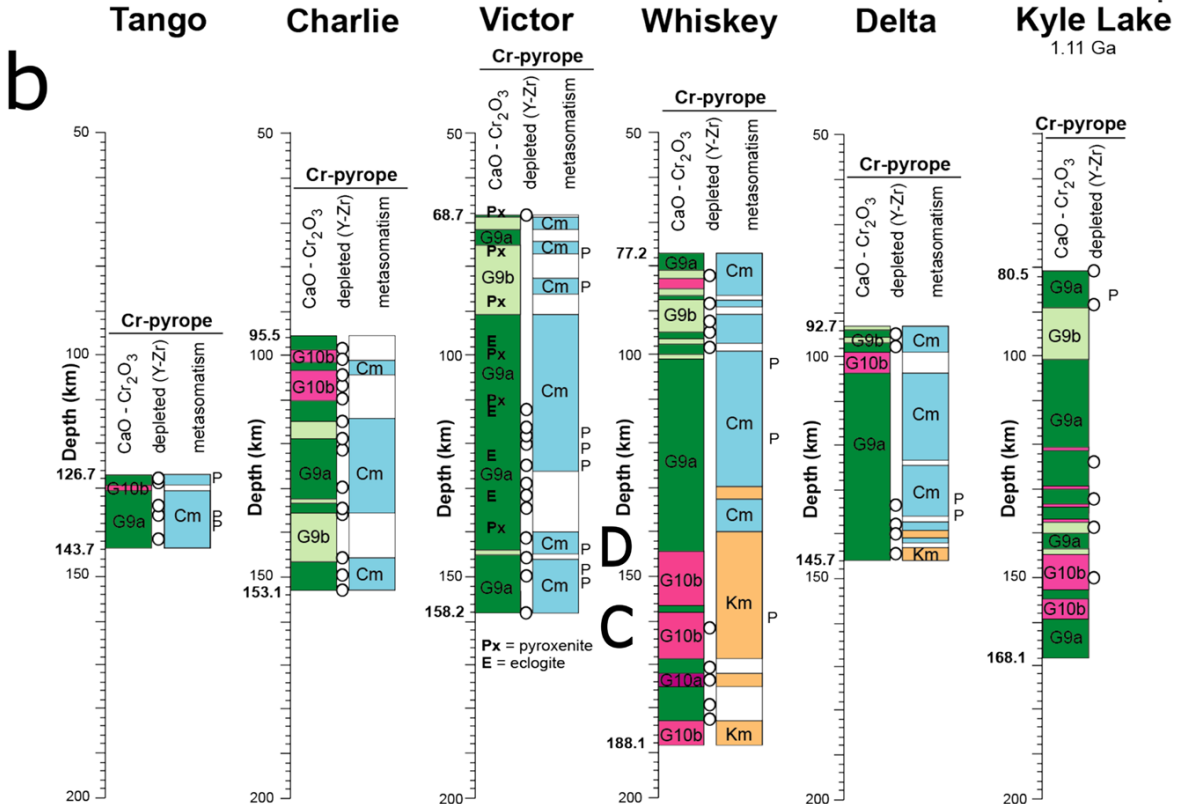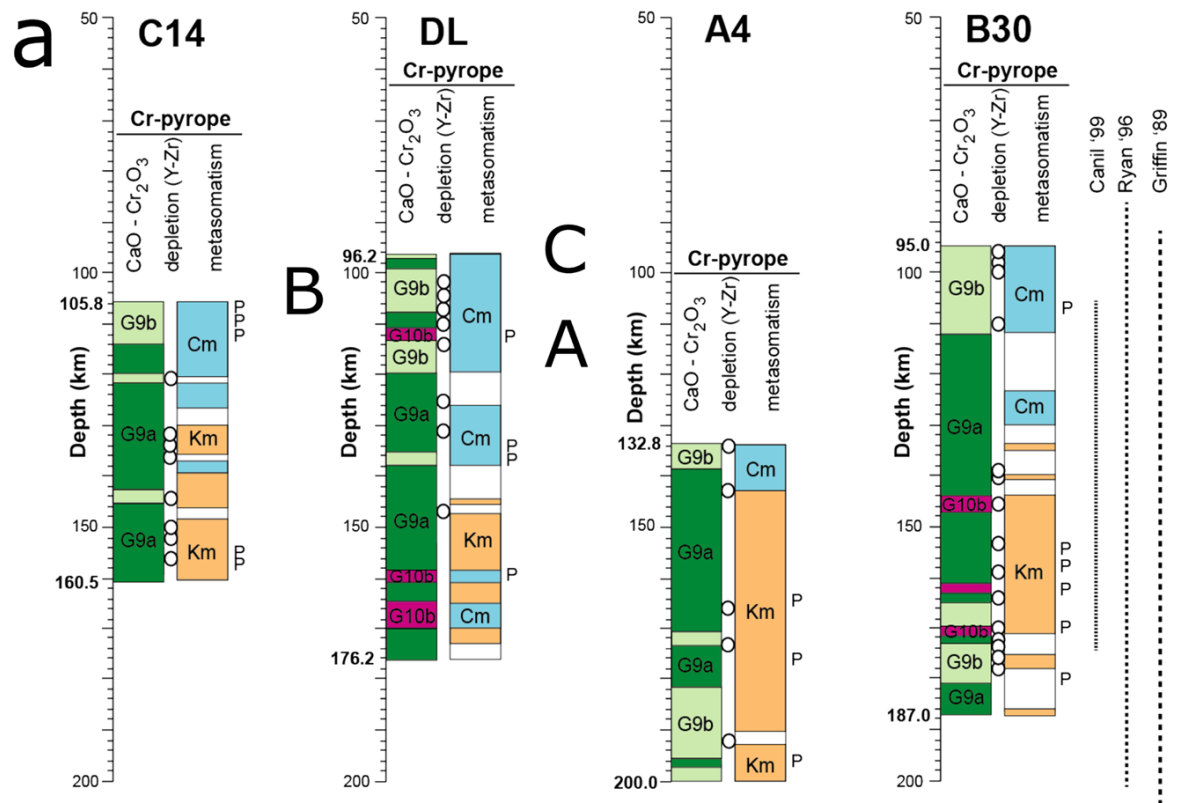
Figure 5. *(a) Kirkland Lake kimberlite lithology and metasomatism logs. Cm is carbonititic metasomatism, Km is kimberlitic metasomatism. The peridotite garnet sampling interval for B30 is compared with those determined by three different Ni-in-garnet thermometer calibrations converted to depth intervals (dashed lines). Intersection depth of seismic discontinuities A, B, and C are indicated. (b) Attawapiskat kimberlite lithology and metasomatism logs. Intersection depth of seismic discontinuities C and D are indicated.*

10

Stratigraphic depth thickness intervals of < ~ 1 km are not utilized in the visualization. Some previous studies (e.g. Griffin et al, 2004) have combined data from multiple different kimberlite pipes within a kimberlite field, so that sufficient data was available to generate mantle stratigraphic logs based on averages over a 100 °C temperature window, overlapped by 50 °C to smooth local variations. However, based on the study by Preston et al. (2012), significant differences in terms of lithology and metasomatic (Ti) overprinting can be observed between adjacent and closely spaced (i.e. < 15 km) kimberlite pipes within the Orapa kimberlite field, suggesting the approach of combining samples from individual kimberlites in a field is not a valid tactic. Petrological observations from this study support this notion, and garnet data from multiple pipes in the same field have not been combined. Mantle stratigraphic logs for Kirkland Lake and Attawapiskat kimberlite fields are shown In Figures 5 and 6.
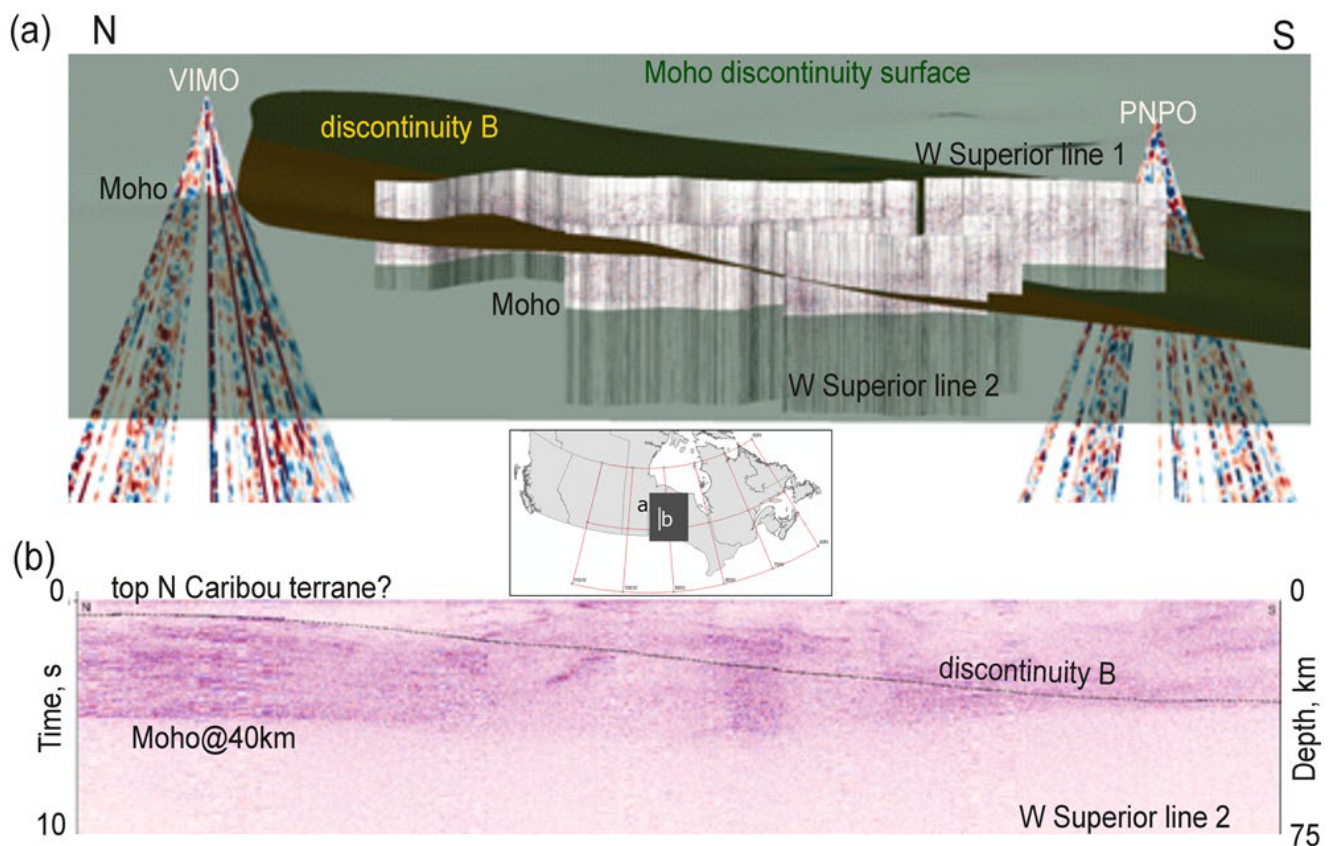
Figure 6. (a) Lithoprobe Western Superior transect deep seismic reflection sections of Lines 1 and 2 embedded in the western part of the Superior 3D model. The view is from high in the west. Line two is about 250 km long. The green-gray Moho surface is nearly horizontal at 40 km depth. (b) Detail of entire Line 2 seismic reflection section. Note that discontinuity B as mapped from receiver functions (e.g., PNPO) intersects these seismic reflection sections either near distinct reflectors (Line 1) or at dipping boundaries between more and less reflective crust; in particular at the north end of Line 2 within the N Caribou terrane (White et al., 2003).

4) Database structure of 3D model

The data is organized by data type in the 3D model. Below indicates the subcategories and datasets. The 3D model is contained in a Gocad project file: *3D_SuperiorMantleModel.prj*.

a) Surfaces:
   i) -Primary surfaces
   ii) -Secondary surfaces
   iii) -Lithoprobe seismic profiles

b) Voxet:
   i) -Bedrock map of Canada (Wheeler et al. 1996) registered at 0 m elevation

c) S-grid:
   i) -Western Superior (Roots and Craven, 2017) and Abitibi Grenville (Roots and Craven, 2017) conductivity models

d) Points:
   i) -Kimberlite lithology
   ii) -Kimberlite metasomatism

e) Curves:
   i) -Graticules: 0m, -100m, -200m

f) Superior Province 3D Model compilation

5) Limitations and uncertainty

As three-dimensional (3D) modelling of the subcontinental mantle lithosphere is increasingly performed with ever more data and better methods, the robustness of such models is increasingly questioned. Resolution thresholds and uncertainty characteristics within deep multidisciplinary 3D models based on geophysical observations exist at a minimum of three levels (Snyder et al., 2018). Seismic waves and potential field measurements have inherent limitations in resolution related to their dominant wavelengths. Formal uncertainties can be assigned to grid-search type forward or inverse models of observable parameter sets. Both of these uncertainties are typically minor when compared to resolution limitations related to the density and shape of a specific observation array used in seismological or potential field surveys. Seismic wave source distribution additionally applies in seismology. A fourth, more complex level of uncertainty relates to joint inversions of multiple data sets. Using independent seismic wave phases or combining diverse methods provides another measure of uncertainty of particular physical properties. Extremely sparse xenolith suites provide the only direct correlation of rock type with observed or modelled physical properties at depths greater than a few kilometers.

Specifically, the Superior mantle model resolution suffers from:
1. Sparse distribution of seismic stations used for correlation of seismic phases in mapping surfaces between stations.

2. Inability to detect vertical structures at relatively high resolution due to the seismic method used.

3. Availability of only two distant xenolith suites.

4. Depth estimates of individual xenoliths or xenocrysts have several kilometers of uncertainty (depending on P-T method adopted); variation intervals less than 2 km were ignored.

5. Low resolution conductivity models due to sparse stations distribution and largely long-period data. We therefore estimate overall uncertainty by observing how well unrelated observations (seismic, MT, xenolith) correlate spatially in a few locations. Such correlations are approximately +/- 10 km.

6) Discussion

Correlations are observed between broad xenolith suite variations with both the receiver function discontinuity surfaces and the resistivity model. The "drill hole" logs of metasomatism show broad correlation between the presence of carbonatitic melt and increased conductivity. Kimberlitic melt correlates with more uniform lherzolite (no eclogites, pyroxenites). The transition zone from one melt to the other correlates with three seismic discontinuities at Kirkland Lake and one at Attawapiskat.

Acknowledgments

References

Aulbach, S., Massuyeau, M., Garber, J. M., Gerdes, A., Heaman, L. M., & Viljoen, K. S. (2020). Ultramafic carbonated melt-and auto-metasomatism in mantle eclogites: Compositional effects and geophysical consequences. Geochemistry, Geophysics, Geosystems, *21*(5), e2019GC008774. https://doi.org/10.1029/2019gc008774.

Bao, X., & Eaton, D. W. (2015). Large variations in lithospheric thickness of western Laurentia: Tectonic inheritance or collisional reworking? Precambrian Research, *266*, 579–586. https://doi.org/10.1016/j.precamres.2015.05.010.

Bedard, J. H., & Harris, L. B. (2014). Neoarchean disaggregation and reassembly of the Superior Craton. *Geology*, *42*, 951–954. https://doi.org/10.1130/g35770.1.

Bedard, J. H., Harris, L. B., & Thurston, P. C. (2013). The hunting of the snArc. Precambrian Research, *229*, 20–48. https://doi.org/10.1016/j.precamres.2012.04.001.

Bostock, M. G. (1998). Seismic stratigraphy and evolution of the Slave province. Journal of Geophysical Research, 103, 21183–21200.

Canil, D. (1999). The Ni-in-garnet geothermometer: calibration at natural abundances. Contributions to Mineralogy and Petrology, 136(3), 240-246.

Daigneault, R., Mueller, W. U., & Chown, E. H. (2002). Oblique Archean subduction: Accretion and exhumation of an oceanic arc During dextral transpression, Southern Volcanic Zone, Abitibi Subprovince Canada. Precambrian Research, *115*(1–4), 261–290. https://doi.org/10.1016/s0301-9268(02)00012-8.

de Kemp, E.A., Russell, H.A.j., Brodaric B., Snyder, D., Hillier M.J., St-Onge M., Harrison, C., Paul, D., Vaillancourt A., Bédard K., Mort A., Schetselaar, E.M., White, D., Logan, C., Ashoori Pareshkoori A., 2022b, Initiating transformative Geoscience practice at the Geological Survey of Canada: Canada in 3D, 2022, Geological Association of Canada/ Mineralogical Association of Canada,

Joint Annual Meeting, Halifax, Canada, May 16th to 18th, 2022. Geological Survey of Canada, Scientific Presentation 141, 2022, 23 pages, https://doi.org/10.4095/331097

Eeken, T., Goes, S., Petrescu, L., & Altoe, I. (2020). Lateral variations in thermochemical structure of the Eastern Canadian Shield. Journal of Geophysical Research: Solid Earth, *125*(7), e2019JB018734. https://doi.org/10.1029/2019jb018734.

Frederiksen, A. W., Miong, S. K., Darbyshire, F. A., Eaton, D. W., Rondenay, S., & Sol, S. (2007). Lithospheric variations across the Superior Province, Ontario, Canada: Evidence from tomography and shear wave splitting. Journal of Geophysical Research: Solid Earth, 112(B7), B07318, doi:10.1029/2006JB004861.

Griffin, W. L., Reilly, S. Y., Doyle, B. J., Pearson, N. J., Coopersmith, H., Kivi, K., Malkovets, V., Pokhilenko, N. (2004). Lithosphere mapping beneath the North American plate. Lithos 77, 873–922. doi:10.1016/j.lithos.2004.03.034 .

Grütter, H. S., Gurney, J. J., Menzies, A. H., & Winter, F. (2004). An updated classification scheme for mantle-derived garnet, for use by diamond explorers. Lithos, 77(1-4), 841-857.

Hunt, L. C., Stachel, T., Grütter, H., Armstrong, J., McCandless, T. E., Simonetti, A., & Tappe, S. (2012). Small mantle fragments from the Renard Kimberlites, Quebec: powerful recorders of mantle lithosphere formation and modification beneath the eastern Superior Craton. Journal of Petrology 53(8), 1597–1635.

Mather, K. A., Pearson, D. G., McKenzie, D., Kjarsgaard, B. A., Priestley, K., (2011). Constraints on the depth and thermal history of cratonic lithosphere from peridotite xenoliths, xenocrysts and seismology. Lithos, 125, 729–742.

Langford, F. F., & Morin, J. A. (1976). The development of the Superior Province of northwestern Ontario by merging island arcs. *American Journal of Science*, *276*(9), 1023–1034. https://doi.org/10.2475/ajs.276.9.1023.

Percival, J. A., Sanborn-Barrie, M., Skulski, T., Stott, G. M., Helmstaedt, H., & White, D. J. (2006). Tectonic evolution of the western Superior Province from NATMAP and Lithoprobe studies. *Canadian Journal of Earth Sciences*, *43*, 1085–1117. https://doi.org/10.1139/e06-062.

Percival, J. A., Skulski, T., Sanborn-Barrie, M., Stott, G. M., Leclair, A. D., Corkery, M. T., Boily, M. (2012). Geology and tectonic evolution of the Superior Province, Canada. Chapter 6 in Percival, J.A., Cook, F.A. Clowes, R.M. (eds.). Tectonic Styles in Canada: The LITHOPROBE Perspective. J. A. Percival, F.A., Cook, R. M Clowes, (eds.). Geological Association of Canada, Special Paper 49, 321–378.

Preston, R. F., Perritt, S. H., Seller, M. H., & Wyatt, B. A. (2012, February). Lithospheric structure beneath the Cretaceous Orapa kimberlite field, Botswana: 4D lithosphere imaging using garnet indicator mineral chemistry. In International Kimberlite Conference: Extended Abstracts (Vol. 10).

Roots, E.A., Hill, G.J., Frieman, B.M., Wannamaker, P.E., Maris, V., Calvert, A.J., Craven, J.A., Smith, R.S. and Snyder, D.B., Magmatic, hydrothermal and ore element transfer processes of the southeastern Archean Superior Province implied from electrical resistivity structure, Gondwana Research, (Vol. 105), 2022, 84-95, https://doi.org/10.1016/j.gr.2021.12.004.

Roots. E.A. and Craven, J.A., 2017. 3D modelling of magnetotelluric data from the western Superior Province, Ontario; Geological Survey of Canada, Open File 8237 (revised), 1 .zip file. https://doi.org/10.4095/306191.

Roots, E.A. and Craven, J.A., 2017. 3D modelling of magnetotelluric data from the Abitibi and Pontiac subprovinces of the Superior Province, Ontario and Quebec; Geological Survey of Canada, Open File 8233 (revised), 1 .zip file. https://doi.org/10.4095/306190.

Ryan, C.G., Griffin, W.L., & Pearson, N.J. (1996). Garnet geotherms: a technique for the derivation of P-T data from Cr-pyrope garnets. Journal of Geophysical Research, 101, 5611-5625.

Sage, R. (2000a). Kimberlites of the Lake Timiskaming Structural Zone: Supplement. Ontario Geological Survey, Open File Report 6018.

Sage, R. (2000b). Kimberlites of the Attawapsikat Area, James Bay Lowlands, Northern Ontario. Ontario Geological Survey, Open File Report 6019.

Schaeffer, A.J., & Lebedev, S. (2014). Imaging the North American continent using waveform inversion of global and USArray data. Earth & Planetary Science Letters, 402, 26–41, doi.org/10.1016/j.epsl.2014.05.014.

Schneider, F. M., Yuan, X., Schurr, B., Mechie, J., Sippl, C., Haberland, C., et al. (2013). Seismic imaging of subducting continental Lower crust beneath the Pamir. *Earth and Planetary Science Letters*, *375*, 101. https://doi.org/10.1016/j.epsl.2013.05.015.

Shu, Q., & Brey, G. P. (2015). Ancient mantle metasomatism recorded in subcalcic garnet xenocrysts: Temporal links between mantle metasomatism, diamond growth and crustal tectonomagmatism. Earth and Planetary Science Letters, 418, 27-39.

Skirrow, R. G., van der Wielen, S. E., Champion, D. C., Czarnota, K., & Thiel, S. (2018). Lithospheric architecture and mantle metasomatism linked to iron oxide Cu-Au ore formation: Multidisciplinary evidence from the Olympic Dam Region, South Australia. Geochemistry, Geophysics, Geosystems, 19(8), 2673–2705.

Smit, K., Pearson, D. G., Stachel, T., & Seller, M., (2014). Peridotites from Attawapiskat, Canada: Mesoproterozoic reworking of Palaeoarchaean lithospheric mantle beneath the Northern Superior superterrane. Journal of Petrology, 55, 1829–1863.

Snyder, D. B., Hillier, M. J., Kjarsgaard, B. A., de Kemp, E. A., & Craven, J. A., (2014). Lithospheric architecture of the Slave craton, northwest Canada, as determined from an interdisciplinary 3D model. Geochemistry, Geophysics, Geosystems, 15(5), 1895–1910.

Snyder, D.B., Schetselaar, E., Pilkington, M. and Schaeffer, A.J., 2018. Resolution and uncertainty in lithospheric 3D geological models. Mineralogy and Petrology, 112(1), 133-147.

Sobolev, 1971. AGU Book Sobolev, N. V. (1971). On mineralogical criteria of a diamond potential of kimberlites. Geologiya i geofizika, 12(3), 70-78.

Vickers, P. (1994) MSc thesis, University of Toronto, Ontario, Canada.

Wang, H., van Hunen, J., Pearson, D. G., & Allen, M. B. (2014). Craton stability and longevity: The roles of composition-dependent Rheology and buoyancy. *Earth and Planetary Science Letters*, *391*, 224–233. https://doi.org/10.1016/j.epsl.2014.01.038.

Wheeler, J O; Hoffman, P F; Card, K D; Davidson, A; Sanford, B V; Okulitch, A V; Roest, W R. Geological Survey of Canada, "A" Series Map 1860A, 1996, 3 sheets; 1 CD-ROM, https://doi.org/10.4095/208175.

White, D. J., Musacchio, G., Helmstaedt, H. H., Harrap, R. M., Thurston, P. C., van der Velden, A., & Hall, K. (2003). Images of a lower-crustal oceanic slab: Direct evidence for tectonic accretion in the Archean western Superior province. *Geology*, *31*, 997–1000. https://doi.org/10.1130/g20014.1.

Appendix

A1 - Data Coordinate system

All receiver function sites, xenolith locations and seismic reference points have NAD83 datum in Canada 3D standard Lambert Conformal Conic projection. Z coordinates are in meter units AMSL, positive upwards. Use the following coordinate system specification for 3D data and GOCAD model components:

Canada 3D Standard Projection

NRCan_Canada_Lambert_Conformal_Conic
Authority: Custom

Projection: Lambert_Conformal_Conic
False_Easting: 0.0
False_Northing: 0.0
Central_Meridian: -95.0
Standard_Parallel_1: 49.0
Standard_Parallel_2: 77.0
Latitude_Of_Origin: 49.0
Linear Unit: Meter (1.0)

Geographic Coordinate System: GCS_North_American_1983
Angular Unit: Degree (0.0174532925199433)
Prime Meridian: Greenwich (0.0)

Datum: D_North_American_1983
Spheroid: GRS_1980
      Semimajor Axis: 6378137.0
      Semiminor Axis: 6356752.314140356
      Inverse Flattening: 298.257222101

A2 – Model and Data

All data and surface models are embedded into a zipped file:

3D_SuperiorMantle.zip
Included is a single SKUA-GOCAD project file, also within a zip file:

  3D.zip
     3D_SuperiorMantleModel.sprj that can be extracted from the publication download file.

     Gocad version details :
     SKUA-GOCAD™ Paradigm-19p4-Applications - Paradigm™ 19

Mantle_Surface/ (Can 3D coordinste system projection)
       Surface_A.ts
       Surface_B.ts
       Surface_C.ts
       Surface_D.ts

Teleseismic_RF/ (Latitude and longitude spherical coordinate system)
       MantleConesStationLocations.csv

       CHGQ_cone.xyzv
       KAPO_cone.xyzv
       KILO_cone.xyzv
       MALO_cone.xyzv
       MATQ_cone.xyzv
       PKLO_cone.xyzv
       PNPO_cone.xyzv
       SILO_cone.xyzv
       SOLO_cone.xyzv
       SUNO_cone.xyzv
       TBO_cone.xyzv
       TIMO_cone.xyzv
       ULM_cone.xyzv
       VIMO_cone.xyzv
       VLDQ_cone.xyzv
       WEMQ_cone.xyzv